

Chemical significance of different temperature regimes for cosmic-ray-induced heating of whole interstellar grains

Juris Kalvāns^{*}, Juris Roberts Kalnin

Engineering Research Institute "Ventspils International Radio Astronomy Centre" of Ventspils University College, Inženieru 101, Ventspils, LV-3601, Latvia

Accepted 2018 Month X. Received 2018 Month Y; in original form 2018 December 7

ABSTRACT

Cosmic-ray-induced whole-grain heating induces evaporation and other processes that affect the chemistry of interstellar clouds. With recent data on grain heating frequencies as an input for a modified rate-equation astrochemical model, this study examines, which whole-grain heating temperature regime is the most efficient at altering the chemical composition of gas and ices. Such a question arises because low-temperature heating, albeit less effective at inducing evaporation of adsorbed species, happens much more often than high-temperature grain heating. The model considers a delayed gravitational collapse of a Bonnor-Ebert sphere, followed by a quiescent cloud core stage. It was found that the whole-grain heating regimes can be divided in three classes, depending on their induced physico-chemical effects. Heating to low-temperature thresholds of 27 and 30 K induce desorption of the most volatile of species – N₂ and O₂ ices, and adsorbed atoms. The medium-temperature thresholds 40, 50, and 60 K allow effective evaporation of CO and CH₄, delaying their accumulation in ices. We find that the 40 K threshold is the most effective cosmic-ray induced whole-grain heating regime because its induced evaporation of CO promotes major abundance changes also for other compounds. An important role in grain cooling may be played by molecular nitrogen as the most volatile of the abundant species in the icy mantles. Whole-grain heating determines the sequence of accretion for different molecules on to grain surface, which plays a key role in the synthesis of complex organic molecules.

Key words: astrochemistry – molecular processes – ISM: cosmic rays – ISM: molecules

1 INTRODUCTION

Cosmic-ray (CR) induced whole-grain heating (WGH) is the result of collisions between interstellar dust grains and CR ions that has an observable effect on the chemistry of interstellar clouds. When a CR particle – typically a relativistic ion – happens to hit a grain, it raises grain temperature by tens of kelvins (Leger et al. 1985). The grain spends only a short time – often a fraction of a second – in the elevated temperature before cooling down to the ambient dust temperature. Yet, the temporal heating facilitates traversing of energy barriers for chemical reactions, diffusion and evaporation for molecules and atoms adsorbed on grain surfaces (d’Hendecourt et al. 1982; Hasegawa & Herbst 1993). Of these, evaporation has the greatest signature on interstellar cloud chemistry.

In nature, WGH occurs for interstellar grains that have

been hit by CRs consisting of a variety of chemical element nuclei with different energies. CR particles usually pass through the grains, only those with energies below ≈ 10 keV may be absorbed in the grains. Grains are being heated to different WGH temperatures T_{CR} , and each T_{CR} has its own occurrence frequency f_T (Kalvāns 2016, hereinafter Paper I), which is equal to the rate at which CRs hit the grain, raising its temperature to T_{CR} . WGH can be accurately described with the help of a temperature spectrum, where each T_{CR} has an attributed frequency f_T . Here we define T_{CR} at a point in time, when the energy from a CR hit has diffused within the whole volume of the grain, which thus has a uniform temperature and before any cooling processes have started to take effect. This time is about 10^{-9} s after the CR hit (Leger et al. 1985).

To the best of our knowledge, there has been no study or even an elaborate estimate comparing the chemical effects of different WGH temperatures. Nevertheless, as a physical process with consequences in chemistry, WGH has been

^{*} E-mail: juris.kalvans@venta.lv

included in many contemporary astrochemical studies (see references in Section 1 of [Kalvāns 2018a](#), hereinafter Paper II). The primary T_{CR} regime used in astrochemical modelling is grain heating to 70 K. This T_{CR} threshold was suggested by [Hasegawa & Herbst \(1993\)](#), probably because such high-temperature grains contain higher amount of thermal energy that can be used for rapid evaporation of volatiles, such as CO. Another T_{CR} threshold is 27 K, the temperature required to induce chemical explosions in irradiated ices ([Greenberg & Yencha 1973](#); [d’Hendecourt et al. 1982](#)). Grain heating to higher temperatures enables more efficient overcoming of energy barriers for molecules adsorbed on grain surface.

Recently, exhaustive studies calculating the WGH temperature spectrum in interstellar clouds have been published (Papers I and II), providing the frequencies f_T for the whole range of T_{CR} possible for interstellar grains. These data show that grain heating to lower WGH temperatures happens more often than heating to higher temperatures. This is because, first, grains are heated more intensively by heavier elements, which are rarer. Second, grains best absorb energy from CRs that have energies in the range 0.2–10 MeV amu^{-1} (Paper I). Considerable energy can also be input by CR ions with energies up to 200 MeV amu^{-1} . The latter interval (10–200 MeV amu^{-1}) has a greater total CR flux because it is larger and the flux density also is growing with CR energy in this region of CR spectra ([Padovani et al. 2009](#); [Chabot 2016](#)). In other words, the cross-correlation of CR energy loss function in grain material and CR energy spectra in clouds results in higher frequencies for grains heated to lower temperatures (see also [de Barros et al. 2011](#)). In addition, grain cooling at low temperatures happens slower than at high temperatures.

These aspects raise the question, whether the regime with the high T_{CR} of 70 K (as assumed by [Hasegawa & Herbst 1993](#)) really is the most efficient in transforming the chemistry of interstellar clouds. The data of Paper II present an opportunity to compare the effects of different WGH temperature regimes with the help of astrochemical modelling. In this study, we aim to clarify the WGH temperature threshold(s) that most profoundly affect the chemistry of interstellar cloud cores. The tasks corresponding to this aim are: deriving analytical formulas for f_T of different T_{CR} regimes from the WGH data from Paper II; implementation of these data in an astrochemical model; calculations with the model; and comparison of modelling results to determine, which T_{CR} regime has the most significant effect on the abundances of key chemical species in gas and ice.

The main novelty of this study arises with the first application of the WGH frequencies from Paper II in an astrochemical model. Clarifying the effects of different WGH regimes is an essential step for understanding the significance of CR-grain interactions. Summarizing the main results of Paper II in analytical formulas will also make our data more accessible to modellers.

Naturally, the adoption of a single WGH temperature is an approximation for the purpose of astrochemical modelling. In fact, the grains are affected by all T_{CR} regimes; moreover, low-temperature WGH arises from less energetic CR hits and from the cooling of higher-temperature grains. Modelling of such cascading and simultaneous processes is

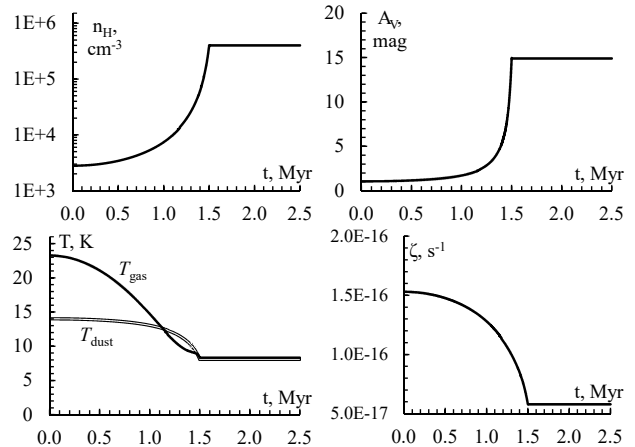


Figure 1. Physical conditions in the modelled central parcel of the cloud core.

a complex task to be performed in a future study. In order to prepare for this task, in the results section we attempted to identify the main physico-chemical processes driving the changes in cloud chemistry, induced by each WGH temperature regime.

2 METHODS

The astrochemical model employed in this study is the latest iteration of the code `ALCHEMIC-VENTA` ([Kalvāns 2015b](#)). An updated approach of WGH frequencies and detailed chemical processes in ices on the heated grains were added to the code.

2.1 Macrophysical model

A suitable macrophysical setting is an important aspect of the model. Authors who have studied the chemical effects induced by CRs acting on interstellar grains ([Hasegawa & Herbst 1993](#); [Shen et al. 2004](#); [Reboussin et al. 2014](#); [Kalvāns 2014](#)) have used pseudo-time dependent models of a cloud with constant density. Similarly to those simulations, a quiescent stage of a dense cloud core was considered also here.

However, in this study, the quiescent stage was preceded by a first stage, where the modelled cloud core contracts. Such a stage was included to examine WGH effects in an environment with changing density. This is necessary because the intensity of CR particles and, thus, the rate of WGH events actually depend on the cloud column density towards the core. The contraction stage starts with hydrogen atom column density N_{H} and numerical density n_{H} characteristic to diffuse molecular gas. These values then increase to the values of the dense, quiescent stage.

The macrophysical model calculates N_{H} towards the centre part of a molecular cloud core. N_{H} was then used for calculating global physical parameters of the modelled gas parcel – interstellar extinction A_V , temperature, and rates

of CR-induced processes. The cloud core was assumed to be surrounded by diffuse gas with isotropic column density $N_{\text{out}} = 5 \times 10^{20} \text{ cm}^{-2}$.

During the first stage, the model traces WGH-induced changes in the chemistry under evolving physical conditions. A $4 M_{\odot}$ Bonnor-Ebert sphere supposedly undergoes a delayed gravitational collapse. The collapse determines the central numerical density of all H atoms (Nejad et al. 1990), starting with $n_{\text{H}} = 2800 \text{ cm}^{-3}$ and increasing to $4 \times 10^5 \text{ cm}^{-3}$ over an integration time $t = 1.5 \text{ Myr}$. Other core parameters were calculated from n_{H} following Equations (1) and (2) of Kalvāns (2018b).

The radius of the contracting sphere decreases from 5.1×10^4 to $3.0 \times 10^4 \text{ AU}$, while N_{H} toward the central parcel of gas increases from 2.1×10^{21} to $3.0 \times 10^{22} \text{ cm}^{-2}$. The initial conditions depict a large and rather diffuse core. Such a size means that its mass is spread over a large volume, resulting in a low initial column density towards the centre of the core, despite a considerable total mass and central density. These geometrical considerations have little effect on the present 0D chemical model, where only the value of A_V is of importance.

The final value of N_{H} is higher than that typical for starless cores (e.g. Lippok et al. 2013) and was chosen to enable analysing results for a medium, where the interstellar radiation field (ISRF) is attenuated and does not hamper the interpretation of WGH-induced chemical effects. In particular, this ensures that desorption is dominated by CR-induced effects.

In the second stage, which lasts another 1.0 Myr, n_{H} and N_{H} are retained constant and equal to those at the end point of the first, contraction stage. This allows to trace chemistry under steady-state conditions. Figure 1 shows the evolution of n_{H} and A_V , which was calculated as $N_{\text{H}}/2 \times 10^{21}$.

The cloud collapse and quiescent core scenarios were intended for simulating conditions encountered in the interstellar medium, relevant to some extent for a variety of objects. The core was assumed to be part of a massive interstellar cloud, where most such cores have been observed. Such a core is partially shielded from incoming radiation by the proximity of sizeable interstellar gas reserves. More precisely, it was assumed that the ISRF photons (and CRs, Section 2.3) can enter the cloud only from two directions, i.e., the core resides in a plane-parallel sheet, irradiated from both sides. This means that the ISRF intensity is reduced by a factor $g/4\pi$, where $g = 2$ is the number of directions the cloud core is exposed to external irradiation. A factor $g = 4\pi$ would characterize a lone, isolated spherical cloud.

During the collapse period, A_V to the centre of the core changes from 1.05 to 14.9 mag. This increase means that the ISRF photons are replaced by CRs and CR-induced photons as the primary drivers of chemical processes in the cloud. The flux of the ISRF photons was taken to be $10^8 \text{ cm}^{-2} \text{ s}^{-1}$, modified by the factor $g/4\pi$ because of geometric effects (see the paragraph above). This corresponds to $2.4 \times 10^{-4} \text{ erg cm}^{-2} \text{ s}^{-1}$. Shielding from the ISRF of H_2 , CO and N_2 molecules was included with the help of tabulated data (Kalvāns 2015b). Gas temperature T_{gas} (Kalvāns et al. 2017) and dust temperature T_{dust} (Hocuk et al. 2017) were calculated as functions of A_V (and thus, N_{H} , see Figure 1). The model considers grains with radius $a = 0.1 \mu\text{m}$ and density 3 g cm^{-3} that constitute 1 per cent of cloud mass.

Table 1. Initial abundances of chemical species relative to H nuclei.

Species	Abundance
H_2	0.5
He	9.00E-2
C	1.40E-4
N	7.50E-5
O	3.20E-4
F	6.68E-9
Na	2.25E-9
Mg	1.09E-8
Si	9.74E-9
P	2.16E-10
S	9.14E-8
Cl	1.00E-9
Fe	2.74E-9

2.2 Chemical model

The model starts with the initial abundances of chemical species listed in Table 1. With the given initial density, the calculated abundances of all chemical species converge to quasi-equilibrium values during the first 0.2 Myr. This is well before an appreciable ice mantle with one monolayer (ML) thickness has formed on grain surfaces at $t = 0.61 \text{ Myr}$. The latter is the first important reference point for a study focusing on surface chemistry.

For the gas chemical network, the model uses the UDfA12 database, which includes binary reactions, ISRF-induced photoreactions, CR-induced ionization and photoreactions (McElroy et al. 2013). The surface chemical network is based on database for complex organic molecules (COMs) by Garrod et al. (2008). It is a reduced version because UDfA12 does not include so many organic species as the COMs network (see also Kalvāns 2018b).

The UDfA12 does not discern between the isomeric radicals CH_2OH and CH_3O , while the COMs network does. Discerning between CH_2OH and CH_3O is important for the synthesis of methanol, a major ice molecule (e.g., Garrod et al. 2008; Vasyunin et al. 2017). We included both radicals in the network. For gas-phase reactions in this regard, data not provided by UDfA12 was adopted from the COMs network.

Neutral species are adsorbed on the inert surface of the grains, forming an icy mantle. The sticking coefficients were calculated according to Thi et al. (2010) for the light species H and H_2 , and taken to be unity for all heavier species. The surface density of adsorption sites was taken to be $1.5 \times 10^{15} \text{ cm}^{-2}$, consistent with an olivine grain (Hasegawa et al. 1992). The mantle was described as consisting of four layers – the surface, ≈ 1 monolayer ($3.5 \times 10^{-8} \text{ cm}$) thick, and three subsurface bulk-ice layers (Kalvāns 2015b). As the MLs accumulate, the surface area of the grain increases accordingly. Total ice thickness can reach a maximum of up to ≈ 100 MLs.

ALCHEMIC-VENTA has been derived from the AL-CHEMIC code, a rate equation model, where surface reactions are treated with the modified rate equation method (Semenov et al. 2010). Bulk-ice binary chemical reactions are permitted (Kalvāns 2015b). Molecular dissociation reactions by ISRF and CR-induced photons in the surface and bulk-ice layers were adopted from the gas phase net-

work (UDfA12). Following the result of Kalvāns (2018b), the photodissociation rates for icy molecules were modified by a factor of 0.3. This is because the efficiency of the photoprocess in ices is lower thanks to neighbouring molecules that help stabilizing excited species. Moreover, nearby dissociation fragments have the possibility of immediate recombination.

In addition to WGH, several surface molecule desorption mechanisms were considered. These are evaporation at the ambient grain temperature T_{dust} , reactive desorption, and photodesorption by ISRF and CR-induced photons. The latter includes also photodissociative desorption. The total (intact and dissociated molecules) photodesorption yield was assumed to be 10^{-3} for most species; for species with available experimental data the yields are listed in Table 3 of Kalvāns (2018b).

2.3 Features different from previous model

In addition to a detailed approach on WGH, several other changes were introduced to the code of Kalvāns (2018b). We employed a 0D (point) version of the model, although the previous iteration of ALCHEMIC-VENTA is 1D. This means that only the central parcel of a cloud core was considered. This change was made to clearly trace changes in specific aspects of cloud chemistry that would not be obvious in a model considering a whole line of sight. Because the central parcel somewhat represents the overall composition of ices along the line of sight towards the centre of the core, a qualitative comparison with observations is possible. cores.

Improvements were made to the micro-physical description of the icy mantles. Following Vasyunin et al. (2017), we assume that the ratio between surface binding energy E_b and desorption energy E_D is 0.55, and that the desorption energy of bulk-ice species is $2E_D$. The rate coefficient for diffusion of icy species between the four mantle layers was updated from that in the original ALCHEMIC-VENTA model of Kalvāns (2015b, Equation (11)). The diffusion rate coefficient is now

$$k_{\text{diff}} = \frac{R_{\text{hop}}}{6l^2}, \quad (1)$$

where R_{hop} is the molecule thermal hopping rate between two adjacent absorption in the icy mantle, l is the average length of a molecule's track (in MLs) before diffusing into an adjacent ice layer and 6 is the assumed number of directions, where a molecule can diffuse to. This means that k_{diff} is now proportional to l^{-2} (instead of l^{-1}), which is more physically correct. As in previous studies with this model, l was taken to be half-thickness of the molecule's current ice layer.

CR-induced ionization rate and photon intensity were adjusted to ensure their compatibility with WGH rates in Section 2.4.3. CRs are attenuated by interstellar matter (Indriolo et al. 2009; Padovani et al. 2009). Taking this into account, the CR-induced ionization rate ζ (s^{-1}) was calculated as a function of N_{H} with initial spectra adopted from Ivlev et al. (2015), model 'High'. The same CR spectra was employed for the WGH rates in Papers I and II. To obtain ζ , the calculated rate was modified by $g/4\pi$, much like the ISRF. Figure 1 shows the resulting evolution of ζ . The flux of CR-induced photons F_{CRph} is proportional to ζ . Following Cecchi-Pestellini & Aiello (1992), it was taken to be

$4875 \text{ cm}^{-2} \text{ s}^{-1}$ when $\zeta = 1.7 \times 10^{-17} \text{ s}^{-1}$. This means that

$$F_{\text{CRph}} = 2.868 \times 10^{20} \times \zeta. \quad (2)$$

2.4 Whole-grain heating and associated processes

2.4.1 General considerations

Hasegawa & Herbst (1993) divided the time grains spend in the elevated WGH temperature with the time interval between energetic CR hits and found that grains spend a part of about 3.2×10^{-19} of their lifetime in a heated state. With the conditions given in this paper, a $0.1 M_{\odot}$ interstellar gas parcel of a cloud contains about 1.6×10^{44} $0.1 \mu\text{m}$ grains. This means that about 5×10^{25} grains would be in a heated state at any given instant. Compared to newer data, Hasegawa & Herbst underestimate WGH frequency for interstellar clouds. Also, grain heating to lower temperatures happens more often and the grains cool slower. For example, grain heating to 27 K happens with a characteristic frequency $f_{>27} \approx 10^{-10} \text{ s}^{-1}$ (Section 2.4.3), while the cooling time-scale is about an hour (Section 2.4.5). This means that 6×10^{37} grains have temperatures close to 27 K at a given time instant. The WGH-affected grains cool, while others are heated, forming a continuously existing population of grains (and their icy mantles) that have a specific WGH temperature T_{CR} .

The above means that, for the purpose of astrochemical modelling, the WGH-affected icy species can be considered as a separate ice phase. The whole WGH process is divided in three stages – heating, molecular-level processes in the heated ices and cooling. The model borrows this approach from Kalvāns (2015a). Molecules in each of the four ice layers at ambient temperature T_{dust} are converted to the same ice layer at WGH temperature T_{CR} with a first-order rate coefficient k_{heat} . The icy molecules at T_{CR} are converted back to molecules in their respective ice layers with a cooling rate coefficient k_{cool} . The abundance of species in the WGH phase is typically eight or more orders of magnitude lower than the abundance of the same species in its respective layer at ambient grain temperature. The coefficients k_{heat} and k_{cool} are discussed below in Sections 2.4.2 and 2.4.5. The molecules in the 'heated ice' phase can diffuse between layers, evaporate and interact via chemical reactions, just like the icy species at the ambient temperature, with the only difference that their temperature is T_{CR} (Section 2.4.4).

This approach on WGH heating is a significant improvement over the original approach of Hasegawa & Herbst (1993) that simply included evaporation with an adjusted rate coefficient. For example, the rate of a process that occurs rapidly at the elevated temperature T_{CR} is controlled by the grain heating and cooling rates, not the inherent rate of such a process.

To investigate the effectiveness of different WGH regimes, several WGH temperature thresholds were considered. These start with the 27 K, the lowest T_{CR} threshold expected to induce significant changes in grain surface processes, and continue with 30, 40, 50, 60, 70, 80, and 90 K thresholds. Together with 'case zero' – a model that does not include WGH – this accounts for a total of nine simulations. As discussed in the results section 3, the WGH thresholds can be divided in three classes, with a 2-3 simulations falling in each class. Therefore, the consideration of

eight WGH regimes allows identification of all or most of the chemical mechanisms and their consequences, induced by WGH.

2.4.2 Data of Paper II

The rate coefficient for ice molecule transition to the icy WGH phase is equal to the frequency of a single grain being heated to T_{CR} , i.e., $k_{\text{heat}} = f_T$. The new, comprehensive data of Paper II allows to distinguish WGH regimes with different minimum T_{CR} thresholds. That study provides tabulated f_T values for the full WGH temperature range for three grain sizes at conditions characteristic to starless cloud cores. These data were adapted for use in this study as described in Section 2.4.3.

For comprehensiveness and because the use of these data provides the main novelty in this paper, we briefly outline the principles used in Paper II to obtain the WGH temperature spectrum. Hasegawa & Herbst (1993) based their estimate of f_{70} – WGH frequency for $T_{\text{CR}} \approx 70$ K – on the frequency of iron CR collisions with interstellar grains. They f_{70} derived from the data of Leger et al. (1985), who employed CR spectra derived in 1970s. More recent and precise interstellar CR energy spectra have been provided, e.g., by Moskalenko et al. (2002); Indriolo et al. (2009); Padovani et al. (2009); Ivlev et al. (2015); Morlino et al. (2015) and Chabot (2016). Their results show that CR intensity drops with increasing column density of interstellar gas and that there is a relatively high flux of low energy CRs with energies < 100 MeV amu $^{-1}$. This had made necessary recalculating the WGH rates. Results of such studies (Chabot 2016, Papers I and II) showed that the grain heating rates can be vastly different from those suggested by Hasegawa & Herbst (1993, see, e.g., the graphic comparison in Figure 9 of Paper II).

Paper II considers dust grains in a molecular cloud, irradiated by CRs with energies in the range 1 eV...10 GeV. The elemental composition of CRs, consisting of 32 different nuclei, was largely adopted from Voyager 1 data (Cummings et al. 2016). The initial CR energy spectra (from Ivlev et al. 2015) was then modified for each nucleus according to the column density of gas traversed by the fast CR ions propagating through the molecular cloud core. In total, eight column densities of H atoms were considered with values relevant to molecular clouds and dense cores. Such dense regions are shielded from the ISRF, which allows accumulating a considerable ice layer on their grains. This changes grain heat capacity, i.e., CR hits with the same energy result in a T_{CR} that is lower for icy grains when compared to naked grain nuclei. This is an additional factor reducing the frequency of high-temperature WGH in dark cores.

The result of the calculations in Paper II is the frequency of CR hits that raise grain temperature to a certain temperature. To obtain the frequency f_T for a minimum T_{CR} threshold, the frequencies for all temperatures above T_{CR} were summed up. For example, $f_{>70}$ is the frequency (s $^{-1}$) of events for a single grain having temperature higher than 70.00 K. The summed frequencies for 0.1 μm grains are listed in Table 4 of Paper II and were used to derive handy analytical functions for the eight T_{CR} thresholds considered in this study (below).

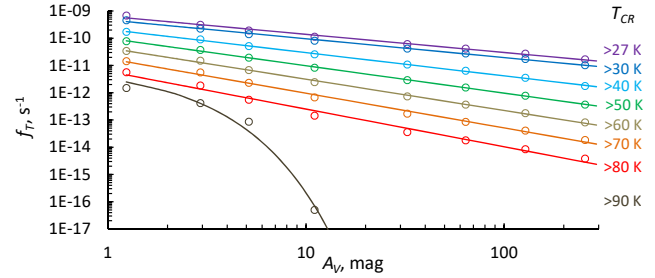


Figure 2. The frequencies f_T for WGH events raising the temperature of a single interstellar dust grain above a certain threshold (T_{CR} regimes). Data points are from Paper II, curves represent the analytical functions defined by Equations 3–9.

2.4.3 Rate of whole-grain heating by CRs

We present analytical formulas from the data of Paper II for the eight WGH temperature regimes. The frequencies f_T are derived for 0.1 μm grains shielded by column densities $2.5 \times 10^{21} \dots 5.1 \times 10^{23}$ cm $^{-2}$, corresponding to interstellar extinctions $A_V \approx 1.2 \dots 256$ mag. The latter values are the maximum application limits for these data because at higher column densities the CR spectra are increasingly modified by spallation and other processes.

According to Paper II, the f_T functions are to be multiplied by the factor $g = 2$, which indicates the extent of external shielding of CRs (Section 2.1). The calculated f_T values are a function of hydrogen column densities, which are here expressed in terms of A_V . It was assumed that $N_{\text{H}}/A_V = 2.0 \times 10^{21}$ cm $^{-2}$.

Figure 2 pictures the f_T functions for different WGH temperature regimes along with data points from Paper II. T_{CR} in Paper II has a built-in accuracy of 0.01; for example, $f_{>27}$ refers to $T_{\text{CR}} > 27.00$ K. The analytical functions themselves are listed below – frequency of WGH events for a single grain that lift its temperature above the T_{CR} threshold.

$$T_{\text{CR}} > 27 \text{ K}; f_{>27} = g \times 3.233 \times 10^{-10} A_V^{-0.6669} \quad (3)$$

$$T_{\text{CR}} > 30 \text{ K}; f_{>30} = g \times 2.364 \times 10^{-10} A_V^{-0.6925} \quad (4)$$

$$T_{\text{CR}} > 40 \text{ K}; f_{>40} = g \times 1.056 \times 10^{-10} A_V^{-0.8527} \quad (5)$$

$$T_{\text{CR}} > 50 \text{ K}; f_{>50} = g \times 4.990 \times 10^{-11} A_V^{-1.007} \quad (6)$$

$$T_{\text{CR}} > 60 \text{ K}; f_{>60} = g \times 2.207 \times 10^{-11} A_V^{-1.148} \quad (7)$$

$$T_{\text{CR}} > 70 \text{ K}; f_{>70} = g \times 9.001 \times 10^{-12} A_V^{-1.273} \quad (8)$$

$$T_{\text{CR}} > 80 \text{ K}; f_{>80} = g \times 3.036 \times 10^{-12} A_V^{-1.383} \quad (9)$$

$$T_{\text{CR}} > 90 \text{ K}; f_{>90} = g \times 4.670 \times 10^{-12} \exp(-1.069 A_V) \quad (10)$$

2.4.4 Chemical processes in the heated ice phase

The effects of processes in CR-heated ices have been analysed before, for the 70 K T_{CR} regime. Hasegawa & Herbst (1993); Roberts et al. (2007) and Iqbal & Wakelam (2018) have studied the effects of WGH-induced evaporation. The

significance of diffusion that facilitates chemical reactions has been studied by [Reboussin et al. \(2014\)](#), while diffusion between ice surface and bulk phases has been considered by [Kalvāns \(2014\)](#). [Kalvāns \(2015a\)](#) analysed the effects of diffusion and reactions, together with CR-induced dissociation of icy species. These studies show that processes other than evaporation affect the abundances of major species only by a few per cent. COMs and other organic molecules can be affected more significantly because of their low absolute abundances.

The approach on the modelling of WGH-induced chemistry was adapted from [Kalvāns \(2015a\)](#) and attributed to the WGH regimes with different T_{CR} . As a separate phase, the species constituting WGH-affected ices have their own physical and chemical processes included in the model. These are evaporation, diffusion between the ice layers, and binary reactions. The rates of these processes were calculated in the same manner as for the icy species, except that they occur at the temperature T_{CR} . For the binary reactions, the same chemical network, based on the COMs database, was used (Section 2.2). The reactions proceed via two steps – the diffusion of reactants and overcoming the reaction activation energy barrier once the reactants have met. Both steps are affected by the elevated temperature. For surface reactions, reactive desorption was considered, too. Photochemistry of the icy molecules in the WGH phase was not included.

2.4.5 Grain cooling

A simple but comprehensive description for grain cooling was employed, suitable for calculating the duration of WGH events for an arbitrary temperature within the relevant T_{CR} interval (up to 90 K). In the model, cooling is a first-order process that converts the molecules in the WGH ice phase with temperature T_{CR} back to the ice phase in the ambient grain temperature T_{dust} . Cooling of the heated grains can occur via evaporation or electromagnetic radiation. Following [Hasegawa & Herbst \(1993\)](#), we assumed that evaporative cooling occurs with the time-scale of CO evaporation t_{evap} . This includes an assumption that there is always a sufficient number of CO molecules on the surface to rapidly cool the grain. The adsorption energy of CO was taken to be 1150 K, from the COMs chemical network. A more precise approach of evaporative grain cooling will be the subject of a dedicated future study.

Radiative grain cooling time-scales depend on grain size and other properties ([Duley 1973](#); [Greenberg & Hong 1974](#); [Aannestad & Kenyon 1979](#); [Tabak 1987](#); [Draine & Li 2001](#); [Cuppen et al. 2006](#)). The radiative cooling time was estimated by integrating equation (15) from [Duley \(1973\)](#) for a temperature interval spanning $0.1T_{\text{CR}}$, centred on T_{CR} . In other words, we assume that the grain resides at the temperature T_{CR} for the time that takes the grain to cool from temperature $1.05T_{\text{CR}}$ to $0.95T_{\text{CR}}$. Such an interval was chosen so that CO and N_2 evaporation rates (the most important processes, induced by WGH) do not deviate by more than about one order of magnitude from these rates at 27 or 30 K at both ends of the interval. These low- T_{CR} regimes are those primarily affected by radiative cooling – the time scale of radiative cooling becomes shorter than that of CO evaporation at $T_{\text{CR}} \approx 31$ K.

Therefore, we obtain that

$$t_{\text{rad}} = \frac{3Nk_B}{2a\sigma A} \times \left(\frac{1}{(0.95T_{\text{CR}})^3} - \frac{1}{(1.05T_{\text{CR}})^3} \right), \quad (11)$$

where N is the number of particles in the grain, k_B is the Boltzmann constant, a is grain radius, σ is the Stefan-Boltzmann constant, and A is grain surface area. N is estimated as the sum of the number of atoms in the amorphous grain nucleus and the number of molecules in the icy mantle. The inclusion of temperatures slightly higher than T_{CR} is adequate because T_{CR} is a minimum temperature threshold for WGH. The main actual effect of radiative cooling is that the energy grain receives from the impacting CR particle is not fully used for breaking bonds between evaporating molecules and grain surface. The total rate coefficient for the cooling process is

$$k_{\text{cool}} = \frac{1}{t_{\text{evap}}} + \frac{1}{t_{\text{rad}}}. \quad (12)$$

3 RESULTS

To determine which T_{CR} regime has the greatest effect on cloud chemistry, the abundances of major species calculated with different T_{CR} regimes were compared to results of ‘model zero’ that does not include WGH. The criterion for ‘major species’ was that their abundance, relative to total hydrogen, $[X] = n_X/n_{\text{H}}$ rises above 10^{-5} for at least one integration step. This criterion was met by CO, CO_2 , H_2O , O_2 , O, N_2 , NH_3 , and N in gas or ice phases. We divide these in oxygen species (Section 3.1) and nitrogen species (3.2). WGH affects also the abundances of more complex minor, organic species, either directly or by altering the proportions of their major parent molecules. This interesting aspect was covered in Sections 3.3 and 3.4.

The abundance curves in the results figures are shown starting with an integration time of 1.0 Myr ($A_V = 3.4$ mag), when surface species have become abundant and WGH is able to influence a significant portion of heavy molecules. During early times, desorption is dominated by ISRF photons. Tables in Appendix A present quantitative data – the calculated abundances of the major species compared to the respective values from the ‘model zero’.

The WGH temperatures, represented in this study by the eight thresholds of T_{CR} (Section 2.4.1), can be divided in several classes. The low-temperature class includes the > 27 and > 30 K regimes. It is efficient at evaporating the most volatile of all species, such as N_2 and O_2 , and also free atoms. The medium T_{CR} class includes the > 40 , > 50 K, and probably > 60 K regimes. These are best at evaporating CO and CH_4 . The high-temperature WGH class includes the > 70 and > 80 K (and, in some cases, > 60 K) regimes that may promote processes with activation energies of up to about 4000 K but generally induce only minor changes to cloud chemistry. The > 90 K regime has a low f_T and the calculated abundances in most cases are identical to the ‘model zero’.

We remind that the studied WGH regimes represent a continuous spectra of WGH temperatures and all the T_{CR} regimes simultaneously affect the composition of interstellar clouds. Nevertheless, we discuss them separately in order to identify key chemical processes induced by each T_{CR} class.

Their understanding will help explaining the cumulative effects of two or more WGH regimes acting simultaneously, to be studied in a future paper. Evaporation has the dominant effect among the WGH-induced processes on the abundances of chemical species.

3.1 Major oxygen species

Oxygen species with $[X]$ higher than 10^{-5} at some point in the simulation are carbon monoxide CO in gas and ice, carbon dioxide CO₂ ice, water H₂O ice and gaseous atomic oxygen O. Slightly below this threshold is gaseous O₂. A quantitative comparison for the calculated abundances of these six species for simulations with all WGH regimes is presented in the appendix tables A1, A2 and A3. Figure 3 shows the calculated abundances for simulations considering different WGH regimes.

O, H₂O, CO and CO₂ form a closely connected gas-ice chemical system. During the first stage of the simulation, gaseous atomic oxygen is transformed to water in the solid phase. The main compounds of carbon are CO in the gas phase and CO and CO₂ in ice. For the temperatures and time-scales characteristic to WGH, H₂O and CO₂ are refractory species and CO is volatile. CO₂ is synthesized only on grain surfaces, usually when CO combines with O or OH. The latter two species are accreted from gas or arise *in situ* from the photodissociation of water ice.

The **medium- T_{CR}** WGH regimes delay the freeze-out of CO for several hundreds of kyr. During this period, the CR-induced dissociation of the CO molecule ensures elevated abundance of C, O and species that are formed from these atoms, including O₂, CH₄ and carbon chains (Section 3.3). Because CO is adsorbed slowly, oxygen preferably accumulates as water ice. CO₂ ice also forms less because of lack of surface CO. Tables A1, A2 and A3 demonstrate that the > 40 K WGH regime is most efficient at inducing these changes.

For the **low-temperature** WGH regimes, heating to the 30 K T_{CR} threshold is able to induce some desorption of CO, while heating to 27 K threshold is not. Both regimes are able to effectively evaporate O₂. The low- T_{CR} WGH class is also efficient at evaporating some of O atoms accreted on surfaces. In the gas, these O atoms may combine into O₂ (and other gaseous species), instead of the refractory water on the surface. Because of this, the highest abundance of O₂ in the gas is reached in the simulations with 27 and 30 K T_{CR} thresholds.

The **high- T_{CR}** regimes are not able to induce drastic changes in oxygen chemistry. The > 70 K and > 80 K simulations have the abundance of gaseous CO increased by a factor of few during the quiescent phase (Table A1), but little in absolute numbers. The abundance of O₂ during the quiescent stage can be increased by up to an order of magnitude above the $[O_2] \approx 4 \times 10^{-11}$ value of the ‘model zero’.

Observationally, WGH-induced desorption can be constrained by analysing the measured proportions of major ice components at different extinctions. The observed abundance ratios of icy CO versus icy H₂O in the interstellar medium are within the range 8–46 per cent (Teixeira & Emerson 1999; Bergin et al. 2005; Whittet et al. 2007, 2011, 2013; Boogert et al. 2011). All simulations produce $[CO]/[H_2O](ice)$ within this range but

the results with medium-temperature WGH thresholds are the closest. For the ratio $[CO_2]/[H_2O](ice)$ observations indicate range 17–44 per cent, which best agrees with simulations with T_{CR} thresholds in the range > 50 to > 80 K, or even the ‘model zero’ (the same references). Figure 4 shows the calculated abundances of CO and CO₂ ices relative to water ice.

3.2 Major nitrogen species

Nitrogen compounds that exceed the 10^{-5} abundance limit are N₂ (gas and ice) and NH₃ (ice), while atomic gaseous N dominates during the early phase of the simulations. Figure 5 shows the calculated abundances of these species, while appendix tables A4 and A5 offer a quantitative comparison, to assess the effectiveness of simulations with different T_{CR} thresholds in transforming the chemistry of nitrogen. These data indicate that the simulations with the 30 K and 40 K WGH threshold again has the most notable effect on the abundances on N species, when compared to ‘model zero’.

CR-induced desorption of N₂ is the primary means how WGH affects nitrogen chemistry in the model. The other major icy nitrogen molecule, NH₃, is refractory at the WGH temperatures. The **low- T_{CR}** WGH class is able to delay the progress of the freeze-out of N₂ by about 300 kyr. The > 30 K regime induces most significant changes in nitrogen chemistry during this freeze-out period. The high abundance of molecular nitrogen also ensures an abundance for atomic N that can be up to three orders of magnitude higher than that of the ‘model zero’. Gaseous N is continuously depleted to the ices in more refractory forms of nitrogen, such as NH₃ and HCN.

The **medium- T_{CR}** class > 40 K and > 50 K regimes are similarly effective at evaporating N₂. After the freeze-out period, which lasts up to $t \approx 1.8$ Myr, gaseous $[N_2] \approx 10^{-7}$, higher than in simulations with other WGH classes and is decreasing till the end of the simulations. The highest increase for gaseous $[N_2]$ for the > 40 K simulation is ≈ 3000 times relative to the abundance calculated with ‘model zero’ at $t = 1.58$ Myr.

The medium WGH class maintain the highest gaseous N₂ abundances during the quiescent stage – the residual gas N₂ abundance at the end of the simulation is higher by a factor of few tens. This is primarily thanks to cosmic-ray induced diffusion between the layers of ice (Section 2.2), which brings some of the subsurface N₂ molecules to the surface, where they are available for desorption. Such a diffusion has a higher energy barrier than evaporation and is not so effective for the low- T_{CR} regimes. The effects of such diffusion show only during the quiescent phase but not in the freeze-out period, when the ice layer experiences rapid growth.

Simulations with the **high- T_{CR}** WGH regimes (here, 60, 70 and 80 K thresholds) show that these are rather inefficient at delaying the accretion of N₂ on grain surfaces, the abundance of gaseous N₂ is increased only by a factor of few (Table A4).

The introduction of WGH has diverse effects on the abundance of solid ammonia, which is the most abundant nitrogen refractory species. During the initial ice accumulation phase up to $t \approx 1.4$ Myr, WGH reduces $[NH_3](ice)$ by a factor of $> 4/5$ because less ammonia is produced via surface dissociation of N₂. This leads to a notable decrease

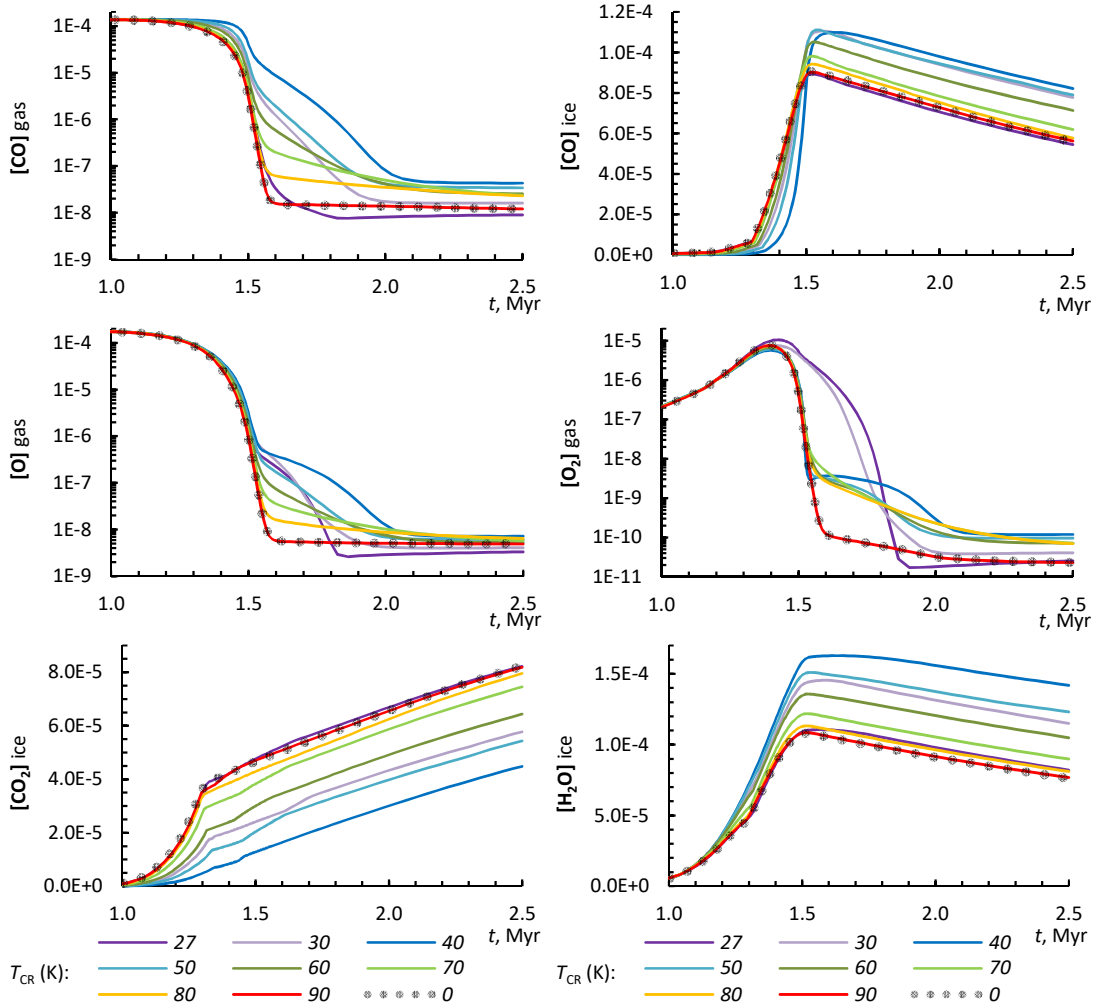


Figure 3. Calculated abundances of major oxygen species (including carbon oxides) in gas and ices from simulations with different T_{CR} regimes. Note that gas-phase abundances are displayed with a logarithmic scale, while those of icy species – with a linear scale. The dots indicate results for ‘model zero’ – a case with no WGH-induced processes.

of (from 19 down to 10 per cent) for the $[\text{NH}_3]/[\text{H}_2\text{O}](\text{ice})$ ratio because $[\text{H}_2\text{O}](\text{ice})$ is increased at the same time (Section 3.2). These variations are most pronounced for the 40 K WGH regime and are within the 2–23 per cent interval for $[\text{NH}_3]/[\text{H}_2\text{O}](\text{ice})$ observed in starless cloud cores (Boogert et al. 2011, 2013, cf. Figure 4). After 1.4 Myr, $[\text{NH}_3](\text{ice})$ is increased at the expense of N_2 ice. This is especially true for the low- T_{CR} regimes during the quiescent stage, when $[\text{NH}_3]/[\text{H}_2\text{O}](\text{ice})$ exceeds 35 per cent. Interestingly, for the low- and medium- T_{CR} regimes, N_2 is the last major molecule to retain significant gas-phase abundance. As nitrogen is accumulated on grain surfaces in the form of NH_3 , the latter molecule covers up to 64 per cent of grain surface.

The abundance of gaseous NH_3 remains within the observational data range of 10^{-9} ... 10^{-7} (e.g., Wirström et al. 2010; Persson et al. 2012; Le Gal et al. 2014) for the whole

duration of the simulations. WGH enhances the relative abundance of gaseous ammonia during the quiescent stage from about 10^{-9} in the ‘case zero’ simulation to 10^{-8} in simulations with 27, 30, 40 and 50 K WGH thresholds. Here, gaseous ammonia is replenished by CR-induced photodesorption, efficient thanks to NH_3 abundance in the outer surface layer of the icy mantles.

3.3 Methane and carbon chains

Methane and species containing the C-C bond are efficiently produced in the gas; freeze-out reduces their gas-phase abundance. Therefore, it can be expected that WGH-induced desorption will increase the gas-phase abundance of these species. In addition, the abundance of the initial source species – gas-phase atomic carbon – depends on CO, which,

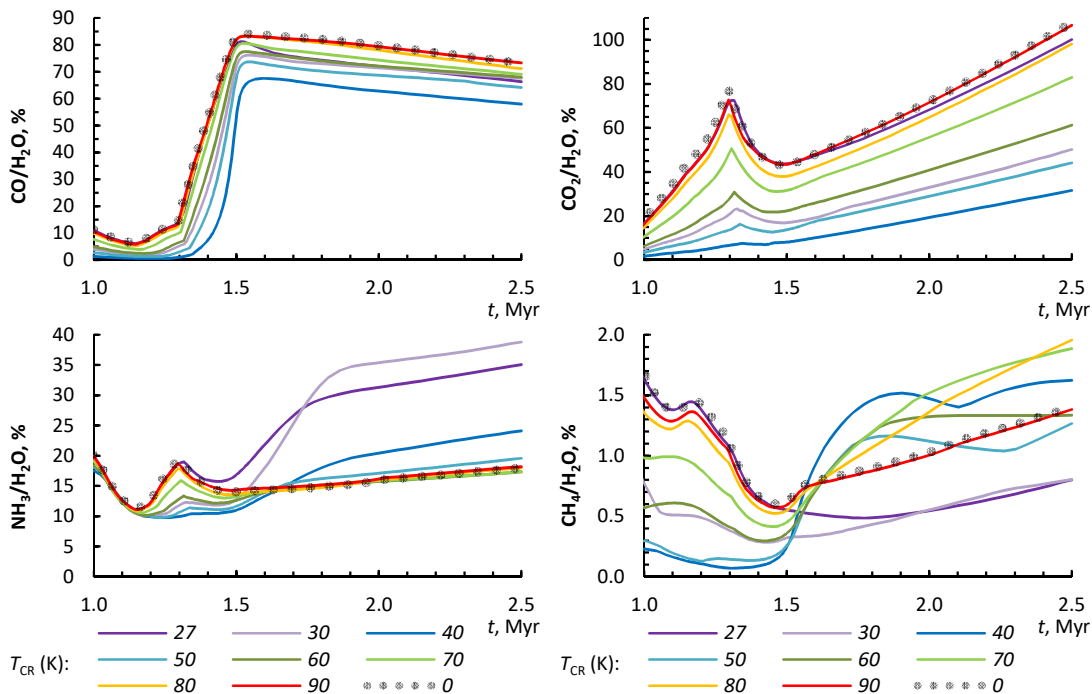


Figure 4. Calculated abundances for important icy species, percentage relative to water ice.

as a volatile molecule, is strongly affected by WGH-induced evaporation.

These general rules are fulfilled with an exception. Figure 6 shows that the **low**-temperature WGH regimes may result in lower abundances of methane or carbon chains during the quiescent phase. For example, $[\text{CH}_4](\text{gas})$ in the no-WGH simulation is stable at around $\approx 4 \times 10^{-10}$. This value is changed in the $T_{\text{CR}} > 27$ K simulation by a factor as low as 0.2. The reduction of gas phase abundance is accompanied with a less pronounced (factor down to 0.6) reduction in abundance of methane ice. More complex species, e.g., C_2H_2 experience larger deviations and similar abundance changes also for the > 30 K regime.

Such a behaviour happens because after the freeze-out of CO, the abundance of C atoms in the gas phase is small, and carbon chains are produced mainly via surface reactions. These are made inefficient by the frequent low- T_{CR} grain heating that causes evaporation of adsorbed C atoms before they can circulate the surface of the grain and combine into molecules.

A similar process occurs also for other WGH regimes but is overshadowed by the effects arising from desorption of CO and other carbon molecules. The **medium** and **high** WGH temperature classes ($T_{\text{CR}} > 40$ to $T_{\text{CR}} > 80$ K) result in methane and carbon chain gas-phase abundances that are order(s) of magnitude higher than those of the ‘model zero’ without WGH. This is because the elevated abundance of CO in the gas and in the surface layer serves as a source for the release of C atoms via dissociation. These atoms are

then involved in gas and surface synthesis of the organics. The above is a classic example, how a process that seemingly involves only major species (CO) has a direct effect on the abundances and observability of minor interstellar species. Therefore, the WGH regime (that with $T_{\text{CR}} > 40$ K) having the most notable effect on CO desorption also most significantly affects the chemistry of carbon chains.

The observed abundance of interstellar methane ice relative to water ice is 0.3–4 per cent (Boogert et al. 1997). This agrees best with the simulations with 70 and 80 K WGH thresholds with $[\text{CH}_4]/[\text{H}_2\text{O}](\text{ice})$ up to 2 per cent, although other simulations can also produce values above 0.3 per cent.

3.4 Complex organic molecules

WGH affects the abundances of COMs in two ways. First, WGH evaporates volatile organics (e.g., COM precursor formaldehyde, see Figure 7), increasing their abundance in the gas phase and hampering their accumulation in ices. Second, WGH changes the rate with which CO ice is accumulated. Subsequent processing of CO-rich ices is a major source of COMs (e.g. Garrod & Herbst 2006). Depending on what species (H_2O , CH_4 , NH_3 , etc.) are co-deposited with CO, some organic species can be preferred over others (Kalvāns 2015c).

Figure 7 shows an example of the latter effect – acetaldehyde CH_3CHO . This molecule is synthesized via the reaction $\text{CH}_3 + \text{HCO}$. While the latter is a direct daughter species of CO, the former (CH_3) arises from methane or

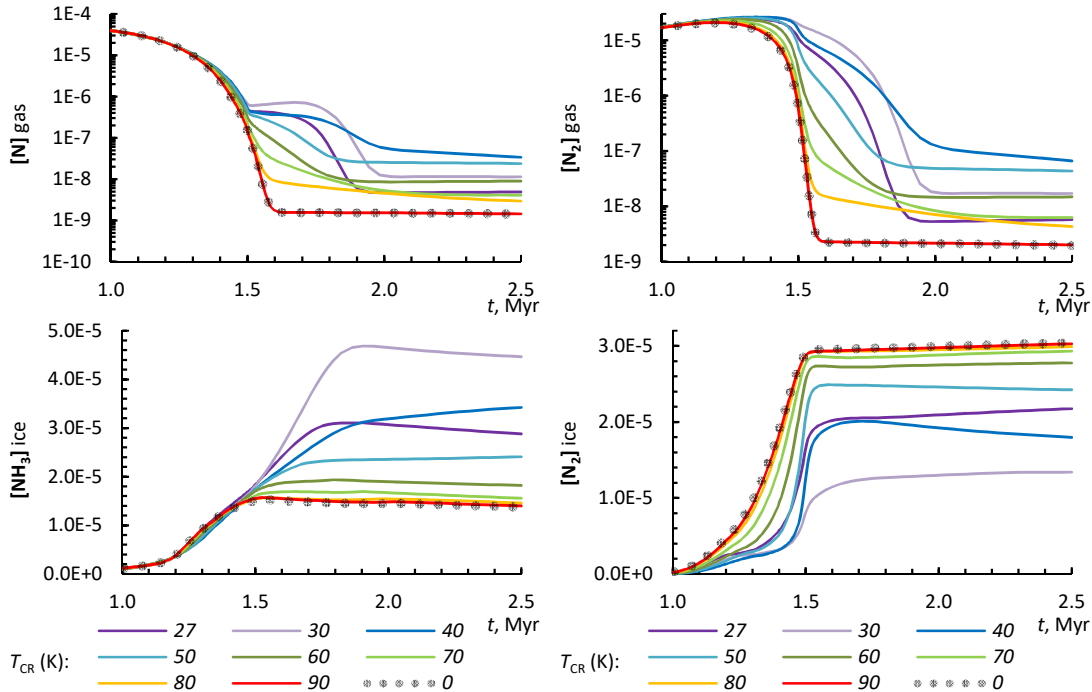


Figure 5. Calculated abundances of major nitrogen species in gas and ices from simulations with different T_{CR} regimes. The dots indicate results for the simulation with no WGH-induced processes.

methanol photodissociation. It happens that for the > 40 K WGH regime, the accretion of CO is delayed, as well as the surface formation of CH_4 , which has a similar desorption energy to CO (cf. top panels of Figures 3 and 6). When the density of the core has reached maximum, these two species accumulate simultaneously, creating an upper ice layer, where their photoprocessing products may interact. This results in conditions that are suited for bulk-ice synthesis of CH_3CHO . For other WGH regimes, such conditions occur to a lesser extent because CO is accreted earlier and the CO-rich layers have more refractory molecules that change the chemical processes. For example, an admixture of H_2O molecules promotes the transformation of CO into the inert CO_2 molecules, instead of organics.

The synthesis of methanol CH_3OH primarily occurs on grain surfaces and directly depends on CO adsorption. Because WGH generally delays the freeze-out of CO ice, the calculated abundances of CH_3OH ice are initially lower than those in the case without WGH for all T_{CR} . Because the accretion of water is not delayed, CO and H_2O are less mixed. This hampers the production of methanol in bulk ice via the combination of CO with atomic H that arises from the photodissociation of H_2O ice.

Despite the effective separation of CO and H_2O for the > 50 K regimes, $[\text{CH}_3\text{OH}]_{\text{ice}}$ increases to about 4.6×10^{-7} (by a factor of three) during the last two hundred kyr (Figure 7). This increase occurs solely in the bulk-ice layer that is closest to outer ice surface. To a lesser extent, the > 40 K simulation shows a similar phenomenon. Such an increase

happens because of a combination of reasons. First, both simulations have characteristic low abundances of hydrogen peroxide because of lack of its parent species – O_2 ice. ($[\text{O}_2]_{\text{ice}}$ is low because O_2 is being kept in the gas phase by the efficient WGH-induced desorption in these simulations.) H_2O_2 in ice is one of the major consumers of atomic H, photo-produced from H_2O . When the supply of H_2O_2 (and NH_2 , another sink of H that is continuously replenished from ammonia) is exhausted, the free H atoms are able to hydrogenate CO in a reaction that has a considerable energy barrier, eventually producing methanol. A major sink of H atoms in ice also is their diffusion to the surface (either as H or H_2) and evaporation. Such diffusion is facilitated by frequent low- T_{CR} heating that occurs also for the simulation with the 40 K threshold. For the 50 K WGH threshold, the diffusion of hydrogen is less efficient, hence H is more involved in chemical reactions, producing the observed increase in the abundance of CH_3OH ice.

The explanation above is specific to the present model of interstellar ices and depends on minute details, such as the assumed desorption energy of hydrogen, mobility of light species in ices, frequency of the WGH events and, of course, the assumed T_{CR} threshold. While it may not work for other models, this illustrates the combinations of chemical and physical processes possible in layered interstellar ices.

Dimethyl ether CH_3OCH_3 is a daughter species of methane and methanol. Its synthesis occurs whenever there is a mix of CH_4 and CO ice. As a hydrogenated surface product, methane forms alongside water in the ‘case zero’ simu-

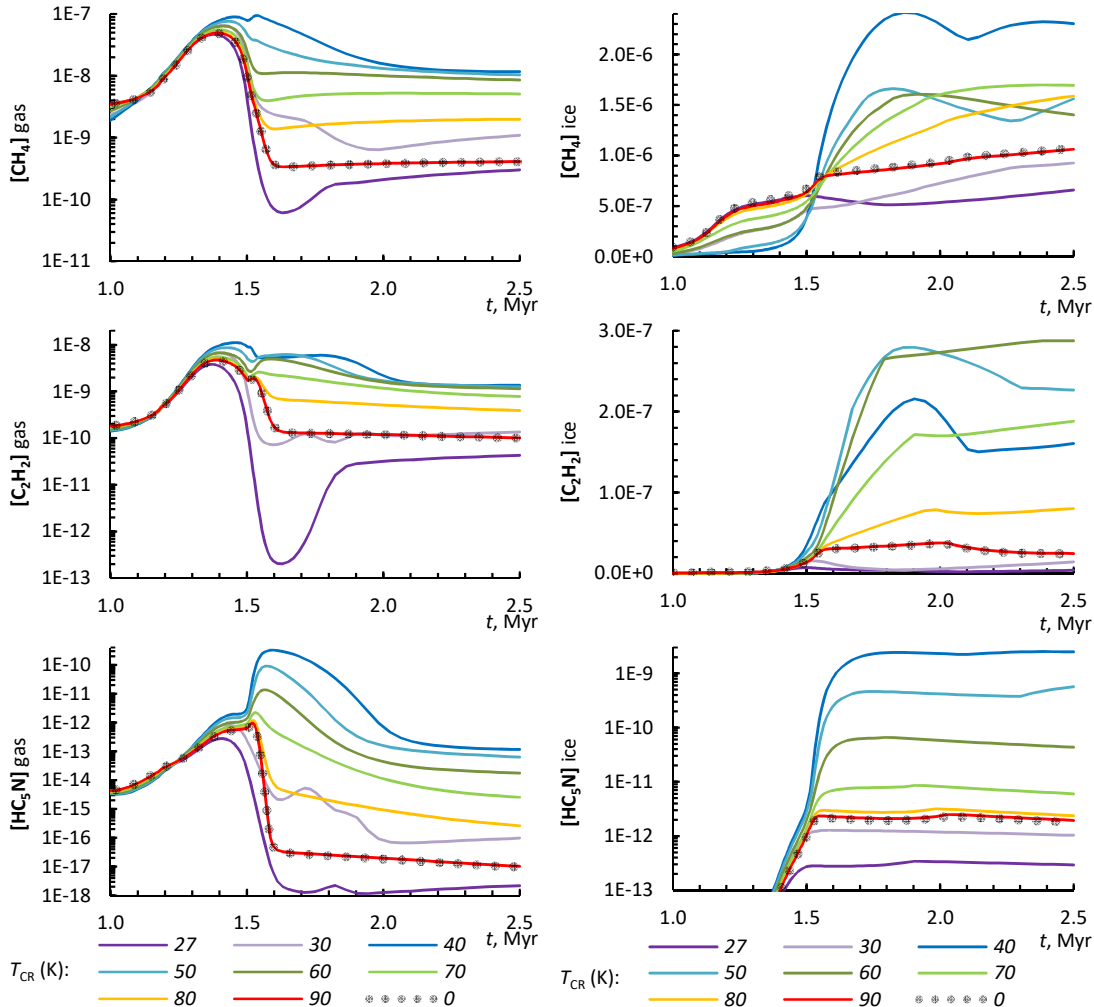


Figure 6. Calculated abundances of methane and example carbon chain species in gas and ices from simulations with different T_{CR} regimes. The dots indicate results for a case with no WGH-induced processes.

lation. However, the introduction of WGH allows methane to co-adsorb with CO. Like in the case of acetaldehyde, this mixture is responsible for the notable increase in the abundance of dimethyl ether for simulations with WGH. The gas-phase abundance of dimethyl ether relative to hydrogen remains low and achieves only 4×10^{-14} for the 40, 50, 60 and 70 K WGH thresholds during the quiescent phase.

The observed abundances of gas-phase organic molecules, such as H_2CO , $HCOOH$, $HCOOCH_3$, CH_3OCH_3 , CH_3O , CH_2CO and CH_3CHO , towards molecular cloud cores often are in the range 10^{-12} – 10^{-9} , relative to hydrogen. Only that of methanol exceeds 10^{-9} (e.g., Öberg et al. 2010; Bacmann et al. 2012; Cernicharo et al. 2012; Vastel et al. 2014). Such a composition might correspond to the proportions of organic molecules in ice, probably indicating a non-selective desorption mechanism at work. The ALCHEMIC-VENTA code is fully able to attain and exceed such abundances for these species in ice (see

also Kalvāns 2015c). However, only volatile species, such as H_2CO , or species that can be rapidly synthesized on grain surfaces ($HCOOH$) attain such abundances in the gas phase during the ice accumulation epoch ($t \approx 1.1$ – 1.6 Myr). We conclude that WGH-induced desorption is not able to explain the observations of COMs in cold cores.

4 CONCLUSIONS

Discussion in Section 3 shows that the chemistry of oxygen, carbon oxides, and nitrogen species is most effectively changed by the > 40 K WGH regime. Regimes with higher T_{CR} thresholds mainly induce changes that are similar to the > 40 K regime but are less pronounced. The low-temperature > 30 K regime is effective at evaporating non-polar small species and introduces specific changes to cloud chemistry, most notably, for nitrogen.

Therefore, we suggest that the > 40 CR-induced WGH

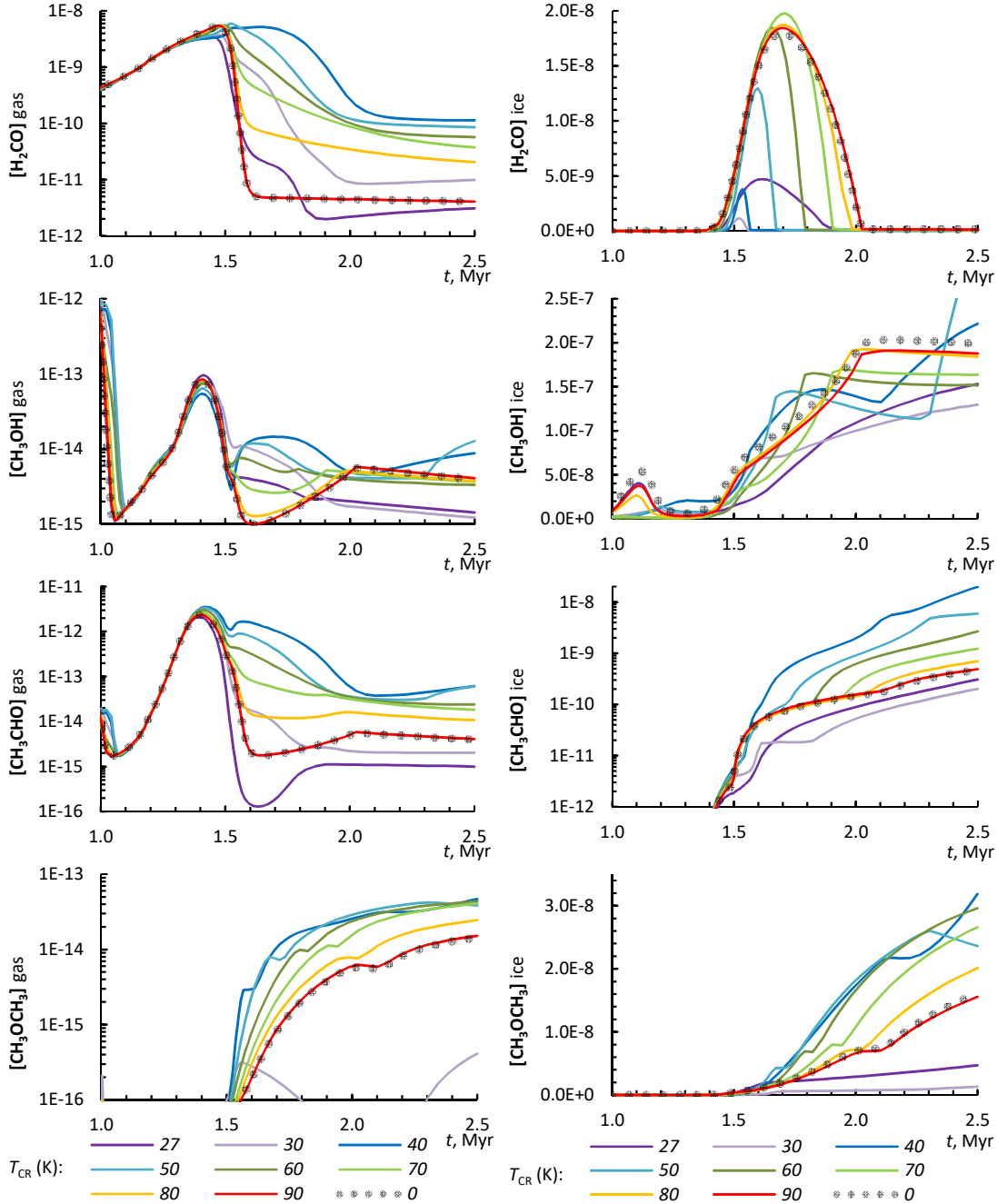


Figure 7. Calculated abundances of selected COMs in gas and ices from simulations with different T_{CR} regimes. The dots indicate results for ‘model zero’ with no WGH-induced processes.

regime should be used in astrochemical modelling with WGH frequency based on updated CR spectra (e.g., as provided in Equation 5). This regime has by far the most notable effect among all WGH regimes on the chemistry of cold cores because it is most efficient at evaporating the CO molecule. In the presented model, such heating is also able

to induce radial diffusion of volatile species in ices, such as N_2 , which amplifies the CR-induced desorption effects.

This paper highlights the necessity for a study considering two or more WGH heating regimes acting simultaneously. As seen in the discussions in Section 3, the chemical consequences of grain heating to even a single WGH temperature can be hardly predictable, with different regimes

sometimes producing opposite effects. The physically relevant cumulative effect on the abundances of interstellar species of several WGH regimes therefore needs to be applied and evaluated. If more than one WGH regime is used in an astrochemical model, then the > 30 and > 50 K regimes should be used next, depending also on the aims of the specific research.

From the results of this study we also conclude that the approach on cooling of grains may have to be modified. All WGH regimes, including the 27 K threshold, induce evaporation of N_2 and O_2 . These molecules are present in the icy mantles of grains in numbers in excess of 10^7 . This is sufficient to control the cooling of grains heated even to 90 K. Like in the case of CO, only a minority of N_2 molecules reside on the outer surface, readily available for evaporative cooling; the time it takes for their diffusion to the surface from the heated ice bulk is another issue.

Finally, we confirmed that a differentiated molecule accretion in ices facilitate the synthesis of some COMs in bulk-ice (see also Kalvāns 2015a). The same process may promote a high gas-phase abundance, as in the case of NH_3 . Both of these ‘secondary’ effects seem to be most pronounced for the > 40 K WGH regime.

ACKNOWLEDGEMENTS

The contribution of JK has been funded by ERDF post-doctoral grant No. 1.1.1.2/VIAA/I/16/194 “Chemical effects of cosmic-ray induced heating of interstellar dust grains”. The contribution of JRK has been supported by ERDF project “Physical and chemical processes in the interstellar medium”, No 1.1.1.1/16/A/213. Both projects are being implemented in Ventspils University College. We thank to Ventspils City Council for support.

REFERENCES

- Aannestad P. A., Kenyon S. J., 1979, *Ap&SS*, **65**, 155
- Bacmann A., Taquet V., Faure A., Kahane C., Ceccarelli C., 2012, *A&A*, **541**, L12
- Bergin E. A., Melnick G. J., Gerakines P. A., Neufeld D. A., Whittet D. C. B., 2005, *ApJ*, **627**, L33
- Boogert A. C. A., Schutte W. A., Helmich F. P., Tielens A. G. G. M., Wooden D. H., 1997, *A&A*, **317**, 929
- Boogert A. C. A., et al., 2011, *ApJ*, **729**, 92
- Boogert A. C. A., Chiar J. E., Knez C., Öberg K. I., Mundy L. G., Pendleton J. J., Tielens A. G. G. M., van Dishoeck E. F., 2013, *ApJ*, **777**, 73
- Cecchi-Pestellini C., Aiello S., 1992, *MNRAS*, **258**, 125
- Cernicharo J., Marcelino N., Roueff E., Gerin M., Jiménez-Escobar A., Muñoz Caro G. M., 2012, *ApJ*, **759**, L43
- Chabot M., 2016, *A&A*, **585**, A15
- Cummings A. C., et al., 2016, *ApJ*, **831**, 18
- Cuppen H. M., Morata O., Herbst E., 2006, *MNRAS*, **367**, 1757
- Draine B. T., Li A., 2001, *ApJ*, **551**, 807
- Duley W. W., 1973, *Ap&SS*, **23**, 43
- Garrod R. T., Herbst E., 2006, *A&A*, **457**, 927
- Garrod R. T., Weaver S. L. W., Herbst E., 2008, *ApJ*, **682**, 283
- Greenberg J. M., Hong S.-S., 1974, in Kerr F. J., Simonson S. C., eds, IAU Symposium Vol. 60, Galactic Radio Astronomy. pp 155–177
- Greenberg J. M., Yench A. J., 1973, in Greenberg J. M., van de Hulst H. C., eds, IAU Symposium Vol. 52, Interstellar Dust and Related Topics. p. 369
- Hasegawa T. I., Herbst E., 1993, *MNRAS*, **261**, 83
- Hasegawa T. I., Herbst E., Leung C. M., 1992, *ApJS*, **82**, 167
- Hocuk S., Szűcs L., Caselli P., Cazaux S., Spaans M., Esplugues G. B., 2017, *A&A*, **604**, A58
- Indriolo N., Fields B. D., McCall B. J., 2009, *ApJ*, **694**, 257
- Iqbal W., Wakelam V., 2018, *A&A*, **615**, A20
- Ivlev A. V., Padovani M., Galli D., Caselli P., 2015, *ApJ*, **812**, 135
- Kalvāns J., 2014, *Baltic Astronomy*, **23**, 137
- Kalvāns J., 2015a, *A&A*, **573**, A38
- Kalvāns J., 2015b, *ApJ*, **803**, 52
- Kalvāns J., 2015c, *ApJ*, **806**, 196
- Kalvāns J., 2016, *ApJS*, **224**, 42 (Paper I)
- Kalvāns J., 2018a, *ApJS*, **239**, 6 (Paper II)
- Kalvāns J., 2018b, *MNRAS*, **478**, 2753
- Kalvāns J., Shmeld I., Kalnin J. R., Hocuk S., 2017, *MNRAS*, **467**, 1763
- Le Gal R., Hily-Blant P., Faure A., Pineau des Forêts G., Rist C., Maret S., 2014, *A&A*, **562**, A83
- Leger A., Jura M., Omont A., 1985, *A&A*, **144**, 147
- Lippok N., et al., 2013, *A&A*, **560**, A41
- McElroy D., Walsh C., Markwick A. J., Cordiner M. A., Smith K., Millar T. J., 2013, *A&A*, **550**, A36
- Morlino G., Gabici S., Krause J., 2015, ArXiv e-print 1509.05128,
- Moskalenko I. V., Strong A. W., Ormes J. F., Potgieter M. S., 2002, *ApJ*, **565**, 280
- Nejad L. A. M., Williams D. A., Charnley S. B., 1990, *MNRAS*, **246**, 183
- Öberg K. I., Bottinelli S., Jørgensen J. K., van Dishoeck E. F., 2010, *ApJ*, **716**, 825
- Padovani M., Galli D., Glassgold A. E., 2009, *A&A*, **501**, 619
- Persson C. M., et al., 2012, *A&A*, **543**, A145
- Reboussin L., Wakelam V., Guilloteau S., Hersant F., 2014, *MNRAS*, **440**, 3557
- Roberts J. F., Rawlings J. M. C., Viti S., Williams D. A., 2007, *MNRAS*, **382**, 733
- Semenov D., et al., 2010, *A&A*, **522**, A42
- Shen C. J., Greenberg J. M., Schutte W. A., van Dishoeck E. F., 2004, *A&A*, **415**, 203
- Tabak R. G., 1987, *ApSS*, **134**, 145
- Teixeira T. C., Emerson J. P., 1999, *A&A*, **351**, 292
- Thi W.-F., Woitke P., Kamp I., 2010, *MNRAS*, **407**, 232
- Vastel C., Ceccarelli C., Lefloch B., Bachiller R., 2014, *ApJ*, **795**, L2
- Vasyunin A. I., Caselli P., Dulieu F., Jiménez-Serra I., 2017, *ApJ*, **842**, 33
- Whittet D. C. B., Shenoy S. S., Bergin E. A., Chiar J. E., Gerakines P. A., Gibb E. L., Melnick G. J., Neufeld D. A., 2007, *ApJ*, **655**, 332
- Whittet D. C. B., Cook A. M., Herbst E., Chiar J. E., Shenoy S. S., 2011, *ApJ*, **742**, 28
- Whittet D. C. B., Poteet C. A., Chiar J. E., Pagani L., Bajaj V. M., Horne D., Shenoy S. S., Adamson A. J., 2013, *ApJ*, **774**, 102
- Wirström E. S., et al., 2010, *A&A*, **522**, A19
- d’Hendecourt L. B., Allamandola L. J., Baas F., Greenberg J. M., 1982, *A&A*, **109**, L12
- de Barros A. L. F., Domaracka A., Andrade D. P. P., Boduch P., Rothard H., da Silveira E. F., 2011, *MNRAS*, **418**, 1363

Table A1. Calculated abundance ratio for the CO molecule in gas and ices: results for simulations with WGH (eight T_{CR} thresholds, listed in the table) versus results without WGH. The latter are provided within the table.

Abundance, no WGH, cm^{-3}	CO gas		CO ice	
	1.5 Myr	2.5 Myr	1.5 Myr	2.5 Myr
	3.67E-06	1.20E-08	8.86E-05	5.58E-05
$(T_{\text{CR}}, \text{K})$	[CO]/[CO no WGH]			
>27	1.20	0.75	0.98	0.98
>30	4.04	1.35	1.13	1.39
>40	12.54	3.59	0.91	1.47
>50	5.47	2.84	1.12	1.41
>60	2.59	2.12	1.12	1.28
>70	1.54	1.98	1.07	1.11
>80	1.15	1.92	1.04	1.03
>90	1.02	1.01	0.99	1.01

Table A2. Calculated abundance ratio for the O atom and the O_2 molecule in gas phase: results for simulations with WGH (eight T_{CR} thresholds) versus results without WGH. The latter are provided within the table.

Abundance, no WGH, cm^{-3}	O gas		O_2 gas	
	1.5 Myr	2.5 Myr	1.5 Myr	2.5 Myr
	1.02E-06	4.91E-09	5.44E-07	2.31E-11
$(T_{\text{CR}}, \text{K})$	[O]/[O, no WGH]		[O_2]/[O_2 , no WGH]	
>27	1.37	0.68	10.16	1.10
>30	2.27	0.83	8.19	1.78
>40	3.30	1.46	1.89	5.15
>50	2.48	1.25	1.85	4.16
>60	1.76	1.08	1.55	3.11
>70	1.32	1.18	1.25	3.11
>80	1.10	1.32	1.07	3.00
>90	1.01	1.00	0.98	0.99

APPENDIX A: COMPARISON TABLES TO ASSESS THE EFFECTIVENESS OF DIFFERENT WGH REGIMES

This appendix presents data calculation results – gas and icy species’ abundances at different WGH regimes – that are quantitatively compared to the results of the ‘model zero’ with no WGH-induced processes at all. The comparison is done for two characteristic points in time – at $t = 1.5$ Myr, when cloud contraction stops, and at $t = 2.5$ Myr, the end time of the modelled quiescent phase.

This paper has been typeset from a $\text{T}_{\text{E}}\text{X}/\text{L}^{\text{A}}\text{T}_{\text{E}}\text{X}$ file prepared by the author.

Table A3. Calculated abundance ratio for the CO_2 and H_2O molecules in the icy mantles: results for simulations with WGH (eight T_{CR} thresholds) versus results without WGH. The latter are provided within the table.

Abundance, no WGH, cm^{-3}	CO_2 ice		H_2O ice	
	1.5 Myr	2.5 Myr	1.5 Myr	2.5 Myr
	4.65E-05	8.23E-05	1.08E-04	7.62E-05
$(T_{\text{CR}}, \text{K})$	[CO_2]/[CO_2 , no WGH]		[H_2O]/[H_2O , no WGH]	
>27	1.02	1.00	1.01	1.08
>30	0.52	0.70	1.32	1.51
>40	0.27	0.54	1.47	1.86
>50	0.44	0.66	1.38	1.61
>60	0.64	0.78	1.25	1.38
>70	0.82	0.91	1.13	1.18
>80	0.92	0.97	1.05	1.06
>90	1.01	0.99	1.00	1.01

Table A4. Calculated abundance ratio for the N atom and the N_2 molecule in gas phase: results for simulations with WGH (eight T_{CR} thresholds) versus results without WGH. The latter are provided within the table.

Abundance, no WGH, cm^{-3}	N gas		N_2 gas	
	1.5 Myr	2.5 Myr	1.5 Myr	2.5 Myr
	1.60E-07	1.42E-09	6.82E-07	1.97E-09
$(T_{\text{CR}}, \text{K})$	[N]/[N, no WGH]		[N_2]/[N_2 , no WGH]	
>27	3.16	3.42	17.03	2.92
>30	4.29	7.96	29.56	8.65
>40	3.53	23.69	24.21	33.53
>50	3.02	16.66	12.29	22.08
>60	2.16	6.28	5.10	7.50
>70	1.50	2.89	2.28	3.18
>80	1.15	2.07	1.33	2.19
>90	1.02	1.01	1.04	1.02

Table A5. Calculated abundance ratio for the NH_3 and N_2 molecules in the icy mantles: results for simulations with WGH (eight T_{CR} thresholds) versus results without WGH. The latter are provided within the table.

Abundance, no WGH, cm^{-3}	NH_3 ice		N_2 ice	
	1.5 Myr	2.5 Myr	1.5 Myr	2.5 Myr
	1.51E-05	1.37E-05	2.89E-05	3.04E-05
$(T_{\text{CR}}, \text{K})$	[NH_3]/[NH_3 , no WGH]		[N_2]/[N_2 , no WGH]	
>27	1.21	2.10	0.56	0.71
>30	1.19	3.26	0.27	0.44
>40	1.15	2.50	0.41	0.59
>50	1.15	1.76	0.69	0.80
>60	1.12	1.33	0.87	0.91
>70	1.06	1.13	0.95	0.96
>80	1.02	1.06	0.99	0.98
>90	1.03	1.02	0.99	1.00